# Discovery, Structure, and Function of Filamentous 3-Methylcrotonyl-CoA Carboxylase

Jason J. Hu[1,2,3,*], Jane K.J. Lee[1,2,4,*], Yun-Tao Liu[1,2,*], Clinton Yu[5], Lan Huang[5], Inna Aphasizheva[6], Ruslan Aphasizhev[6,7], and Z. Hong Zhou[1,2,†]

[1]Department of Microbiology, Immunology, and Molecular Genetics, University of California, Los Angeles (UCLA), Los Angeles, CA 90095, USA

[2]California NanoSystems Institute, UCLA, Los Angeles, CA 90095, USA

[3]Department of Mathematics, UCLA, Los Angeles, CA 90095, USA

[4]Department of Psychology, UCLA, Los Angeles, CA 90095, USA

[5]Department of Physiology and Biophysics, University of California, Irvine, Irvine, CA 92697, USA

[6]Department of Molecular and Cell Biology, Boston University Medical Campus (BUMC), Boston, MA 02118, USA

[7]Department of Biochemistry, BUMC, Boston, MA 02118, USA

*Jason J. Hu, Jane K.J. Lee, and Yun-Tao Liu contributed equally to this article. Order was determined alphabetically by last name.

†Corresponding author and lead contact:

Email: hong.zhou@ucla.edu, Phone: 310-694-7527

## SUMMARY

3-methylcrotonyl-CoA carboxylase (MCC) is a biotin-dependent enzyme necessary for leucine catabolism in most organisms. While the crystal structure of recombinant bacterial MCC has been characterized, the structure and potential polymerization of native MCC remain elusive. Here, we discovered that native MCC from *Leishmania tarentolae* (LtMCC) forms filaments and determined its structure at near-atomic resolution using cryoEM. $\alpha_6\beta_6$ LtMCC dodecamers assemble in a twisted-stacks architecture, manifesting as supramolecular rods extending up to approximately 400 nanometers. LtMCCs in filaments bind biotin but are not covalently biotinylated and lack coenzyme A. Filaments elongate by stacking $\alpha_6\beta_6$ LtMCCs onto the exterior α-trimer of the terminal $\alpha_6\beta_6$ dodecamer. This stacking immobilizes the biotin carboxylase domains, sequestering the enzyme in an inactive state within the mitochondrial matrix. Our results support a new model for LtMCC catalysis, termed the dual-swinging-domains model, and cast new light on the functional significance of polymerization in the carboxylase superfamily and beyond.

## Keywords

3-methylcrotonyl-CoA, carboxylase, cryoEM, filament, leucine catabolism, biotin, mitochondria, Leishmania, atomic modeling, cryoID

## INTRODUCTION

3-methylcrotonyl-CoA carboxylase (MCC) is a biotin-dependent enzyme necessary for the catabolism of leucine (Anderson et al., 1998; Knappe et al., 1961; Nikolau et al., 2003), an essential branched-chain amino acid involved in regulating cellular metabolism (Gondáš et al., 2022; Yang et al., 2010), protein synthesis (Gondáš et al., 2022; Yang et al., 2010), and anabolic signaling (Gran and Cameron-Smith, 2011; Paulussen et al., 2021). MCC belongs to a superfamily of biotin-dependent carboxylases with different substrate preferences, such as acetyl-CoA carboxylase (ACC), geranyl-CoA carboxylase (GCC), propionyl-CoA carboxylase (PCC), and pyruvate carboxylase (PC). In eukaryotes, MCC resides in the mitochondrial matrix (Tong, 2013). Documented in many species (Diez et al., 1994; Gallardo et al., 2001; Höschle et al., 2005), MCC shares high cross-species sequence homology (Figure S1). In humans, upregulated MCC expression often correlates with various cancers (Chen et al., 2021; Dai et al., 2020; Gondáš et al., 2022; He et al., 2020; Liu et al., 2019). On the other hand, MCC deficiency, one of the most common metabolic disorders in newborns (Lee and Hong, 2014), may cause vomiting, seizures, and other neurological abnormalities (Grünert et al., 2012; Kim et al., 2017).

As part of the mitochondrial leucine degradation pathway, MCC catalyzes the conversion of 3-methylcrotonyl-CoA to 3-methylglutaconyl-CoA (Gallardo et al., 2001). Upon covalent biotinylation of the apoenzyme, MCC accelerates two successive reactions: biotin carboxylation and carboxyl group transfer (Lynen et al., 1961; Moss and Lane, 1971). First, biotin is carboxylated at an α-subunit active site with bicarbonate as the carbon dioxide donor upon concomitant ATP hydrolysis (Lynen et al., 1961; Moss

43 and Lane, 1971; Tong, 2013). Next, the carboxylated biotin is translocated to the
44 corresponding β-subunit active site, where the carboxyl group is transferred from biotin
45 to 3-methylcrotonyl-CoA (Lynen et al., 1961; Moss and Lane, 1971; Tong, 2013).
46 The atomic structure of bacterial MCC has been solved by X-ray crystallography
47 using recombinant *Pseudomonas aeruginosa* MCC ($PaMCC^{rec}$) expressed in
48 *Escherichia coli* with His-tags to the β-subunits (Huang et al., 2012). $PaMCC^{rec}$ subunits
49 oligomerize into a dodecameric complex with a core of six β-subunits sandwiched by
50 two α-trimers in an $\alpha_6\beta_6$ architecture (Huang et al., 2012). Whether MCCs may exist in
51 other forms is unclear. Albeit, their supramolecular assembly was conjectured based on
52 rod-shaped aggregations of *Achromobacter* IVS MCC observed by negative-stain
53 electron microscopy (Apitz-Castro et al., 1970). Recent advances in cryogenic electron
54 microscopy (cryoEM) have uncovered unexpected modes of enzyme polymerization
55 and elucidated the regulatory roles of such architectural forms (Lynch et al., 2017;
56 Mattei et al., 2020; Maud et al., 2022; Park and Horton, 2019; Wang et al., 2019; Webb
57 et al., 2017). For example, near-atomic resolution cryoEM structures illuminated the
58 regulatory functions of several filamentous forms of eukaryotic ACC (Hunkeler et al.,
59 2018). In the absence of high-resolution structures of the native MCC enzyme, it
60 remains unsettled whether native MCCs can similarly form supramolecular assemblies.
61 Here, we used a bottom-up structural proteomics cryoEM approach (Ho et al.,
62 2020; Pfab et al., 2021) to identify and determine the near-atomic resolution structure of
63 native *Leishmania tarentolae* MCC (LtMCC) enriched from mitochondrial fraction by
64 streptavidin affinity pulldown. We discovered that LtMCC filaments consist of stacks of
65 LtMCC $\alpha_6\beta_6$ dodecamers. The biotin carboxylase (BC) domains of adjacent $\alpha_6\beta_6$

66 dodecamers bind with each other, inhibiting their mobility. In contrast, at the filament
67 termini, the BC domain is flexible, while the linker between the biotin carboxyl carrier
68 protein (BCCP) and the BC-CT mediating (BT) domain is rigid. These observations
69 support a dual-swinging-domains model for LtMCC catalysis and suggest a regulatory
70 role of LtMCC filamentation in the mitochondrial matrix.

71 **RESULTS**

72 Discovery and identification of LtMCC filaments from mitochondrial lysate

73 While examining complexes enriched by sedimentation of mitochondrial lysate from
74 parasitic protist *L. tarentolae* in 10%-30% glycerol gradient (Figure 1A) and affinity
75 pulldown with streptavidin-coated magnetic beads, we serendipitously discovered
76 filamentous structures (Figure 1B). We identified the constituents of these filamentous
77 structures by following the workflow detailed in Figures 1B–1C, which is based on the
78 cryoID bottom-up structural proteomics approach (Ho et al., 2020). Using single-particle
79 reconstruction, we obtained two differently centered cryoEM maps of the filament
80 middle segments, one at 3.4 Å and another at 3.9 Å resolution (Figure 1B). Additionally,
81 we processed the termini particles and found that the two termini have the same
82 structure, which was resolved at 7.3 Å resolution (Figure 1B).

83 To establish the protein identities of the cryoEM maps, we first obtained a partial
84 model prediction from DeepTracer (Pfab et al., 2021) using the 3.9 Å map. The
85 sequence of the output model from DeepTracer (Pfab et al., 2021) was then input into
86 cryoID (Figure 1C). Searching for proteins detected by mass spectrometry (Table S1),
87 cryoID identified LtMCC α-subunits as a filament component. Upon visual inspection, it
88 was clear that the filaments also contain LtMCC β-subunits. Indeed, LtMCC α- and β-
89 subunits produced the most peptide spectral counts of all proteins detected by mass
90 spectrometry (Table S1). Furthermore, we ruled out GCCs as the filament components
91 because GCCs are not found in eukaryotes (Waldrop et al., 2012). We built the atomic
92 model for the filament *de novo*, using an AlphaFold (Jumper et al., 2021; Mirdita et al.,
93 2022) predicted model for the α-subunit and the β-subunit as references. We found that

both the 3.4 Å and 3.9 Å maps contain the same subunits but center on the β- and α-subunits, respectively. After translating one map for half of an $\alpha_6\beta_6$ stack along the filament and a slight rotation around the filament axis, the two maps match well with one another (cross-correlation coefficient of 0.74). The slightly better resolution of the map centered on the β-subunits is probably because the architecture of the β-subunits is more stable.

## Structure of native eukaryotic LtMCC filaments

LtMCC filaments are predominantly straight (Figure 2A) although some are curved (Figure 2B), with a maximum observed curvature reaching 3.1 $\mu m^{-1}$. With a mean length of 993 Å, the length distribution resembles a Poisson distribution (Figure 2C), similar to that of ACC filaments isolated from animal tissues and observed by negative stain electron microscopy (Kleinschmidt et al., 1969). Most filaments consist of four to six $\alpha_6\beta_6$ dodecamers, or stacks (Figure 2C). With an architecture similar to that of $PaMCC^{rec}$, each $\alpha_6\beta_6$ stack in the LtMCC filament is characterized by an $\alpha_6\beta_6$ cylindrical dodecamer exhibiting D3 symmetry (Figure 2D). Measuring to a height of 216 Å and width of 148 Å, the dodecamer is composed of a core of six β-subunits (β-core) sandwiched by two layers of trimeric α-subunits (Figure 2D, Video S1). Modeling the atomic structures of LtMCC $\alpha_6\beta_6$ stacks into our cryoEM reconstruction reveals that the filament has a twisted-stacks architecture; that is, neighboring $\alpha_6\beta_6$ stacks are related by a rotation of 23° and a translation of 216 Å (Figure 2D). In the filament, the active sites are exposed in both α- and β-subunits (indicated by stars in the middle panel of Figure 2D).

117 Each α-subunit contains the BC, BT, and BCCP domains, and two linkers: the
118 BC-BT linker and the BT-BCCP linker, the latter of which was unmodeled in PaMCC$^{rec}$
119 (Figures 2E). A prominent feature of the BC domain is the presence of two large central
120 β-sheets surrounded by α-helices. The active site of each α-subunit is located inside the
121 central pocket of the BC domain (Figure 2F) and is responsible for carboxylating BCCP-
122 bound biotin. In contrast to the BT domain of PaMCC$^{rec}$, which contains a central α-helix
123 accompanied by a seven-stranded antiparallel β-barrel (Huang et al., 2012), the LtMCC
124 BT domain features eight β-strands (Figure S2). When the dodecameric PaMCC$^{rec}$ and
125 LtMCC are superimposed globally, the BC, BT, and BCCP domains in LtMCC are
126 rotated with respect to those in PaMCC$^{rec}$ (Figure S3A–B). However, when individual
127 domains are superimposed independently, they fit well with each other (Figure S3C–E),
128 suggesting that the above observed structural differences between the LtMCC filament
129 and PaMCC$^{rec}$ are likely due to filamentation.
130 Like in PaMCC$^{rec}$, each LtMCC β-subunit possesses an N-carboxyltransferase
131 (N-CT) domain and a C-carboxyltransferase (C-CT) domain. We have designated two
132 new domains in LtMCC: the N-dock domain and CT-linker (Figure 2E), located before
133 and after the N-CT domain, respectively. The N-dock domain was introduced to
134 facilitate description of interactions between α- and β-subunits in the filament (see
135 below). Designating the helix-loop-helix-loop fragment between the N-CT and C-CT
136 domains as a separate domain (CT-linker) renders the N-CT and C-CT domains to have
137 near-identical backbone folds (Figure S4), despite sharing only 19% sequence identity.
138 Each of the six β-core active sites is wedged at the N-CT and C-CT interface between a
139 top and a bottom β-subunit (Figures 2G, 3A) and is responsible for carboxylating 3-

140 methylcrotonyl-CoA. Similar to that in PaMCC$^{rec}$, each LtMCC β-core active site is
141 roughly 80 Å away from its corresponding α-subunit active site.
142
143 LtMCC filaments bind biotin but lack coenzyme A
144 PaMCC$^{rec}$ was crystalized as both a holoenzyme (with bound CoA and covalently-linked
145 biotin) and an apoenzyme (without CoA and biotin). By contrast, $\alpha_6\beta_6$ stacks in the
146 LtMCC filament contain non-covalently-bound biotin but lack CoA (Figure 3A). For
147 LtMCC to perform its two-step catalytic process, covalent biotinylation must occur first.
148 Although biotin is observed at the expected β-core active sites, it is untethered to
149 Lys651 in the highly conserved Ala-Met-Lys-Met sequence in the BCCP domain.
150 Indeed, the carboxyl group of biotin is about 10 Å apart from the ε-amino group of
151 Lys651 (Figure 3A), which is too far to form a prosthetic group (Moss and Lane, 1971).
152 The existence of non-biotinylated BCCP domains in LtMCC filaments suggests that the
153 filamentous LtMCC is inactive. Similarly, inactive forms of PCC also bind biotin without
154 forming a covalent adduct (Arabolaza et al., 2010; Diacovich et al., 2004).
155 The bicyclic ring system in biotin consists of an ureido ring and a thiophane ring
156 (Hu and Cronan, 2020). Carboxylation requires the transfer of the carboxyl group
157 attached to the N1′ atom of the biotin uredo ring to acyl-CoA (Knowles, 1989).
158 Therefore, the orientation of the N1′ atom of biotin is important for carboxylation. In
159 LtMCCs, the N1′ atom in the ureido ring of biotin is proximal to the CoA binding site, but
160 not in PaMCC$^{rec}$ (Figure 3A). This is because the biotin bicyclic ring in LtMCC is
161 approximately 180° rotated relative to that of PaMCC$^{rec}$ (Figure 3B). The spatial
162 arrangement of LtMCC biotin is consistent with PCC biotin (Huang et al., 2010;

163 Scheffen et al., 2021) and PC biotin (Fry et al., 1985) (Figure 3B). In contrast, the
164 arrangement of PaMCC$^{rec}$ biotin is consistent with ACC biotin (Huang et al., 2012; Wei
165 and Tong, 2015) (Figure 3B). Therefore, biotin orientation is variable at the β-core active
166 site for different carboxylases and carboxylases in different catalytic states.
167

168 α-subunits associate more with β-subunits than with intra-trimer α-subunits

169 Many interactions are observed between an α-subunit and the β-core, with 1,515 Å$^2$ of
170 buried surface area as calculated by ChimeraX (Goddard et al., 2018) and a binding
171 affinity of -11.7 kcal mol$^{-1}$ as calculated by PRODIGY (Vangone and Bonvin, 2015; Xue
172 et al., 2016). Interactions between each α-subunit and the β-core are mainly mediated
173 by a hook between the central α-helix and β1 strand of one BT domain that curls into a
174 groove of a β-subunit (yellow segment from Asp494–Thr506 in Figure 4A). This groove
175 is formed by the N-CT, C-CT, and N-dock domains (Figure S5). Due to its shorter
176 sequence, the LtMCC hook contains only one hairpin in contrast to two hairpins in the
177 PaMCC$^{rec}$ hook (Figure S2). In both structures, the hook is crucial for interactions with
178 the β-subunit to reinforce inter-subunit associations (Huang et al., 2012). The additional
179 structures resolved in our cryoEM map also unveil previously unrecognized associations
180 among domains of three neighboring subunits: the BT-BCCP linker of an α-subunit, N-
181 dock domain of a β-subunit, and N-CT domain of another β-subunit (Figure 4B). Here,
182 the BT-BCCP linker "docks" onto the crescent N-dock domain (Figure 4B).

183 Fewer interactions are observed between intra-trimer α-subunits, contributing just
184 579 Å$^2$ of buried surface area and a binding affinity of -6.1 kcal mol$^{-1}$. Within an α-trimer,
185 each α-subunit interacts with its neighboring α-subunits through the BC-BC and BC-BT

186 interfaces. At the BC-BC interface, a loop from one BC domain (Glu34–His36) interacts
187 with a loop (Phe379–Pro385) and a helix (Arg423–Gln427) from a neighboring BC
188 domain (Figure 4C). At the BC-BT interface, strand β6 (Gly572–Ala581) from the β-
189 barrel in the BT domain interacts with a short β-strand (Ala59–Cys61) in the BC domain
190 through β-sheet augmentation (Harrison, 1996) (Figure 4D).
191

192 ## Structure of filament termini reveals mechanism of LtMCC polymerization

193 To investigate the mechanism of LtMCC polymerization, we reconstructed the filament
194 termini at 7.3 Å resolution (Figure 5A). We found that both ends of the filament
195 terminate at α-trimers, with partially resolved densities attributed to the BC domains
196 (Figure 5A). When displayed at a high threshold, cryoEM densities for the BC, BCCP
197 domain, and the BC-BT linker disappear, while density for the BT domain and BT-BCCP
198 linker of the same α-subunit remain visible (Figure 5A). Therefore, the weaker densities
199 of the BC and BCCP domains are due to their flexibility, rather than low occupancy of
200 the α-subunit at the termini, which would make all domains of the α-subunit disappear.
201 The flexibility of the BC and BCCP domains is further supported by limited intra-trimer α-
202 subunit associations (Figures 4C–D). In contrast, the BT-BCCP linker is mostly rigid as
203 it interacts extensively with the β-subunits (Figure 4B).
204 Our observation that LtMCC filaments terminate at α-subunits suggests that the
205 building block for the filament is an $\alpha_6\beta_6$ stack. Filaments plausibly elongate one stack at
206 a time, attaching through BC domains to form an α-α interface (Video S2), which is
207 defined as the associations between two α-trimers from adjacent stacks (Figure 5B).
208 The α-α interface has a total buried surface area of 1,689 $Å^2$ and a binding affinity of -

209 11.6 kcal $mol^{-1}$. At the α-α interface, the BC domain of an α-subunit from the lower α-
210 trimer interacts with the BC domains of two α-subunits from the upper α-trimer (Figure
211 5B). Interactions contributing to the α-α interface occur primarily between loops, along a
212 local twofold axis (right panel of Figure 5B): the first site of interaction is between two
213 loops (Leu338–Asp344), with its neighboring residues Lys319 and Arg231 also
214 participating in α-α interactions; the second site of interaction occurs between two loops
215 connected to two α-helices (His257–Glu261). These interactions at the α-α interface
216 stabilize the BC domains between neighboring stacks in the LtMCC filament (Figure
217 5B).

218 ## DISCUSSION

219 This study reveals an important, yet previously unrecognized role of the BC domain in
220 MCC catalysis. During catalysis, the BCCP domain must shuttle biotin between the CT
221 active site (β-subunit) and the BC active site (α-subunit), located approximately 80 Å
222 apart (Figure 5A). However, we observed that the BT-BCCP linker is fixed (Figure 5A).
223 Therefore, the maximum distance that the BCCP domain can translocate by itself is
224 about 60 Å, which is insufficient for the BCCP domain to reach the BC active site (right
225 panel of Figure 5A). As such, for catalysis to occur, both the BCCP and active-site-
226 containing BC domain must move so that BCCP-bound biotin can reach the BC active
227 site. Indeed, at the filament termini, the BC domain is flexible, thus permitting BC
228 domain movement. We term this the dual-swinging-domains model to highlight the
229 difference from the original swinging-domain model (Tong, 2013), in which only the
230 BCCP domain swings. Beyond MCC, both the BCCP and BC domains have been
231 documented to move in pyruvate carboxylase (Maurice et al., 2007; Xiang and Tong,
232 2008). These observations suggest that carboxylase catalysis in general may involve a
233 dual-swinging domains mechanism.

234 In LtMCC filaments, the α-α interface fixes the BC domain, thus preventing its
235 swinging. According to our dual-swinging-domains model, immobilization of the BC
236 domain inhibits catalysis. Therefore, filamentation likely sequesters LtMCCs in a
237 quiescent state in the mitochondrial matrix (Figure 5C), which may provide a capacity to
238 reactivate the enzyme in response to environmental signals. Polymerization appears to
239 be a readily deployable and economic mechanism for regulating the activity of abundant
240 mitochondrial matrix enzymes in response to rapid changes in cellular metabolism

241 requirements. Such capacity is particularly relevant for parasitic protists cycling between
242 the amino acid-rich gut environment of insect vectors and the high glucose
243 concentration in the bloodstream of their hosts.

244 Our inquiries into MCC polymerization further reflect the diversity of
245 polymerization in the carboxylase superfamily. It is known that both isoforms of ACC,
246 ACC1 and ACC2, form filaments (Beaty and Lane, 1983; Hunkeler et al., 2018; Kim et
247 al., 2010; Kleinschmidt et al., 1969; Meredith and Lane, 1978; Park et al., 2013; Wei
248 and Tong, 2018). Recently, high-resolution structures of filamentous ACC1 have been
249 reported (Hunkeler et al., 2018). In contrast to LtMCC, ACC1 assembles into two
250 filamentous forms: an active single-stranded and inactive double-stranded helical
251 structure. Eukaryotic MCC and ACC filamentation exhibit different architectures and
252 regulatory functions, supporting the distinct evolutionary lineages of these enzymes
253 (Huang et al., 2012). Nonetheless, filament formation may be a general way to regulate
254 enzymatic activity in the carboxylase superfamily.

255 Evolutionarily, employing the same gene costs less than “inventing” a new gene
256 for regulation. Polymerization is a remarkable example of such a cost-effective strategy.
257 In the case of LtMCC, the stacking of active $\alpha_6\beta_6$ dodecamers can inhibit biotin shuttling
258 (Figure 5C), thus sequestering enzymes by polymerization. In other enzymes,
259 polymerization can alter specificity (Kim et al., 2005), increase activity (Polley et al.,
260 2019), and even introduce non-enzymatic functions such as conducting electrons
261 between bacterial cells (Wang et al., 2019) and regulating cell curvature (Ingerson-
262 Mahar et al., 2010). Just like how complex life forms arose by the aggregation and

263 polymerization of unicellular forms, the diverse functions arising from enzyme

264 polymerization can be considered as a rudimentary form of evolution.

265 ## STAR★METHODS

266 ### KEY RESOURCES TABLE

| REAGENT or RESOURCE | SOURCE | IDENTIFIER |
|---|---|---|
| **Experimental models: Organisms/strains** | | |
| *L. tarentolae* TATII/UC strain | (Parrot, 1949) | TATII/UC was isolated from Algerian gecko in 1939 and maintained in axenic culture in various laboratories. Parasite culture used in this study was received from Prof. Larry Simpson laboratory at UCLA in 2004 and transfected with pX based plasmid expressing RNA editing ligase 1 (KREL1). |
| **Chemicals, peptides, and recombinant proteins** | | |
| Complete protease cocktail tablet | Roche | Sigma product no: 11836170001 |
| **Software and algorithms** | | |
| MotionCorr2 | (Zheng et al., 2017) | https://emcore.ucsf.edu/ucsf-software |
| Gctf | (Zhang, 2016) | https://www2.mrc-lmb.cam.ac.uk/research/locally-developed-software/zhang-software/#gctf |
| RELION 3.1 | (Zivanov et al., 2018) | https://www3.mrc-lmb.cam.ac.uk/relion/index.php/Main_Page |
| ChimeraX | (Goddard et al., 2018) | https://www.cgl.ucsf.edu/chimerax/ |
| Coot | (Emsley et al., 2010) | https://www2.mrc-lmb.cam.ac.uk/personal/pemsley/coot/ |
| Phenix | (Liebschner et al., 2019) | https://phenix-online.org/ |

| | | |
|---|---|---|
| DeepTracer | (Pfab et al., 2021) | https://deeptracer.uw.edu/ |
| cryoID | (Ho et al., 2020) | https://github.com/EICN-UCLA/cryoID |
| ESPript 3 | (Robert and Gouet, 2014) | https://espript.ibcp.fr/ESPript/ESPript/ |
| AlphaFold | (Jumper et al., 2021; Mirdita et al., 2022) | https://github.com/sokrypton/ColabFold |
| IMOD | (Kremer et al., 1996) | https://bio3d.colorado.edu/imod/ |
| SerialEM 3.8 | (Mastronarde, 2005) | https://bio3d.colorado.edu/SerialEM/ |
| ExPASy Translate | (Gasteiger et al., 2003) | https://web.expasy.org/translate/ |
| Clustal Omega | (Sievers and Higgins, 2018) | https://www.ebi.ac.uk/Tools/msa/clustalo/ |
| PRODIGY | (Vangone and Bonvin, 2015; Xue et al., 2016) | https://wenmr.science.uu.nl/prodigy/ |
| ResMap | (Kucukelbir et al., 2014) | http://resmap.sourceforge.net/ |
| **Deposited data** | | |
| Crystal Structure of PaMCC$^{rec}$ apoenzyme | (Huang et al., 2012) | PDB: 3U9T |
| Crystal Structure of PaMCC$^{rec}$ holoenzyme | (Huang et al., 2012) | PDB: 3U9S |
| Crystal Structure of PCC D422-mutant β-subunit | (Arabolaza et al., 2010) | PDB: 3IB9 |
| Crystal Structure of PCC wild-type β-subunit | (Diacovich et al., 2004) | PDB: 1XNY |
| CryoEM Structure of ACC–Citrate filament | (Hunkeler et al., 2018) | PDB: 6G2D |
| CryoEM Structure of ACC–BRCT filament | (Hunkeler et al., 2018) | PDB: 6G2I |
| Crystal structure of ACC holoenzyme | (Wei and Tong, 2015) | PDB: 5CSL |

| | | |
|---|---|---|
| Crystal structure of PCC holoenzyme | (Huang et al., 2010) | PDB: 3N6R |
| CryoEM map of α-subunit centered LtMCC | This paper | EMDB: XXXX |
| CryoEM map of β-subunit centered LtMCC | This paper | EMDB: XXXX |
| CryoEM map of LtMCC termini | This paper | EMDB: XXXX |
| CryoEM structure of the LtMCC filament | This paper | PDB: XXXX |
| **Other** | | |
| MagStrep XT beads | IBA Lifesciences | 2-4090-002 |
| Zeba™ Spin Desalting Columns | Thermo Fisher Scientific | Catalog number: 89882 |

## RESOURCE AVAILABILITY

### Lead contact

Further information and requests for resources and reagents should be directed to and will be fulfilled by the lead contact, Z. Hong Zhou (hong.zhou@ucla.edu).

## EXPERIMENTAL MODEL AND SUBJECT DETAILS

*L. tarentolae* cells were grown at 27°C in brain heart infusion media supplemented with 5 mg/L of hemin and harvested during late-exponential growth phase at ~$2x10^8$ cell/ml.

## METHOD DETAILS

### Preparation of mitochondrial lysate

279 Mitochondrial fraction was enriched by hypotonic cell lysis and sequential separation of
280 membrane-containing fraction on RenoCal76 density gradients (Pelletier et al., 2007).
281 Mitochondrial pellets (0.5-0.8 g wet weight) were lysed in 1 ml of pH 7.3, 50 mM
282 HEPES, 150 mM KCl, 2 mM EDTA, 1% NP40, and 50 µl of 20x Complete protease
283 cocktail by sonication at 24W for 15 seconds and centrifuged at 30,000 RPM in an
284 SW55 rotor for 15 minutes. The supernatant was recovered and separated on a
285 continuous 10-30% gradient glycerol in pH 7.3, with 20 mM HEPES, 100 mM KCl, and 1
286 mM EDTA and prepared in SW28/32 Setton clear tubes for 15 hours at 72,000 g.
287 Glycerol gradient fractions of 1.5 ml were collected from the top and those
288 corresponding to 20S-40S region were combined.
289
290 **Purification of LtMCC by streptavidin affinity pulldown**
291 Glycerol gradient fractions were supplemented octylglucoside to 2 mM and incubated
292 on Strep-Tactin®XT magnetic beads in a Binding Buffer (50 mM Tris-HCl, pH 8.0, 100
293 mM KCl, 1 mM EDTA, 2 mM OG) for 1 hour at 4°C on a nutating mixer. Beads were
294 washed with 5 ml of Binding Buffer twice. For elution, the beads were incubated in 0.2
295 ml of Elution Buffer (20 mM Tris-HCl, pH 8.0, 100 mM KCl, 1 mM EDTA, 2 mM OG, 100
296 mM biotin) at 4°C for 10 minutes. The 130 µl of purified material was exchanged into
297 Sample Buffer (20 mM Tris-HCl, pH 7.5, 60 mM KCl, 5 mM $MgCl_2$, 1 mM DTT, 5 mM
298 OG) using Zeba™ Spin Desalting Columns, 7K MWCO (0.5 ml). The sample was then
299 centrifuged at 21,000g for 10 minutes and the supernatant was stored on ice before grid
300 preparation.
301

302 **Protein identification by LC-MS/MS**

303 Affinity-purified complexes were sequentially digested with LysC peptidase and trypsin.
304 LC-MS/MS was carried out by nanoflow reversed phase liquid chromatography (RPLC)
305 using an UltiMate 3000 RSLC (Thermo Fisher Scientific) coupled on-line to an Orbitrap
306 Fusion Lumos mass spectrometer (Thermo Fisher Scientific). A cycle of full FT scan
307 mass spectrum (m/z 375-1500, resolution of 60,000 at m/z 400) was followed by
308 MS/MS spectra acquired in the linear ion trap for 3 seconds at top speed with
309 normalized collision energy (HCD, 30%). Following data extraction to MGF format using
310 MSConvert from ProteoWizard (Chambers et al., 2012), resultant peak lists for each
311 LC-MS/MS experiment were submitted to Protein Prospector (UCSF) for database
312 searching (Fang et al., 2012). Each project was searched against a normal form
313 concatenated with the random form of the *L. tarentolae* Parrot Tar II from the TriTrypDB
314 database (Amos et al., 2022). The mass accuracy for parent ions and fragment ions
315 were set as ± 10 ppm and 0.6 Da, respectively. Trypsin was set as the enzyme, with a
316 maximum of two missed cleavages allowed. Cysteine carbamidomethylation was set as
317 a fixed modification, and protein N-terminal acetylation, methionine oxidation, and N-
318 terminal conversion of glutamine to pyroglutamic acid were selected as variable
319 modifications.

320

321 **CryoEM sample preparation**

322 Lacey carbon cryoEM grids with a 2 nm continuous carbon film (Ted Pella) were first
323 glow discharged for 45 seconds with a target current of 15 mA, using PELCO
324 easiGlowTM. Then a 2.5 µL sample was applied to the grids. After waiting for 5

325 seconds, the grids were blotted for 4 seconds with blot force 0, at 100% humidity and
326 4°C temperature; after blotting, the grids were plunge-frozen into liquid ethane using an
327 FEI Mark IV Vitrobot (Thermo Fisher Scientific). The grids were stored in a liquid
328 nitrogen dewar before imaging.
329
330 **CryoEM image acquisition**
331 The cryoEM grids were loaded and imaged using a Titan Krios (Thermo Fisher
332 Scientific) operated at 300 kV, with a Gatan K3 camera and a Gatan Imaging Filter
333 Quantum LS. Movies were recorded with SerialEM (Mastronarde, 2005) by electron
334 counting in super-resolution mode at a pixel size of 0.55 Å/pixel. The exposure time was
335 2 seconds and fractionated to 40 frames. The defocus range was between -1.5 to -2.5
336 μm. The total dosage was approximately 40 electrons/Å2. A total of 3,328 movies were
337 collected.
338
339 **CryoEM image processing**
340 The movies were processed with MotionCor2 (Zheng et al., 2017), leading to dose-
341 weighted and drift-corrected electron micrographs with a calibrated pixel size of 1.1 Å.
342 We discarded the first frame due to severe drift of this frame. The defocus of the
343 micrographs was determined by Gctf (Zhang, 2016). Using IMOD (Kremer et al., 1996),
344 the micrographs were binned by a factor of 10 to make a stack for particle picking. After
345 directly observing filaments on the micrographs, we manually picked the start and end
346 of each filament using the 3dmod command in IMOD (Kremer et al., 1996). A total of
347 4,496 filaments were picked. To derive the constituents of the filaments, we coded a

Python script to subdivide the filaments into equally spaced segments of 87 Å. The coordinates were then converted through a Bash script to RELION format. A total of 51,322 particles were extracted in total through RELION 3.1, with a box size of 384.

After extraction, we performed reference-free 2D class averaging on the particles with RELION 3.1 (Zivanov et al., 2018). We chose the best classes and proceeded to 3D classification. We made an initial 3D model from the best 3D class averages through RELION 3.1. The 3D classification was done with D3 symmetry and yielded α- and β-centered 3D class averages. After removing duplicates, the α- and β-centered classes contained 7,582 and 13,250 particles, respectively. We did 3D refinement for the α- and β-centered map independently with D3 symmetry using RELION 3D refinement. We then performed CTF refinement for both maps independently using RELION 3.1. We used CTF refinement (Zivanov et al., 2018) to improve the accuracy of the defocus for each particle and to correct beam tilt for the dataset. After performing CTF refinement, we performed 3D refinement for both maps again, independently. At the end of all processing, based on RELION's gold-standard Fourier shell correlation (FSC) at the 0.143 criterion, we obtained α- and β-centered maps at 3.9 and 3.4 Å resolution, respectively (Figure S6). The resolution towards the center of the map is better than the edge of the map (Figure S6).

For the filament termini map, we used RELION 3.1 to extract the previously picked filament start-and-end points at a box size of 384 pixels. We calculated the in-plane rotation angle using the direction of vectors from the start to end of the filament. We used a Python code to include the in-plane rotation angle information in the RELION star file for the particles. We performed 2D classification for these particles without local

371 search around the precalculated in-plane rotation angle. To generate an initial 3D
372 model, we used the IMOD clip function (Kremer et al., 1996) to change the center of the
373 β-centered map. The best particles were selected for 3D reconstruction with C3
374 symmetry. We performed 3D classification and removed bad particles. During 3D
375 classification, we set the "limit_tilt" parameter to 85 to keep side-view particles. We
376 proceeded to 3D refinement with 3,380 particles. We obtained a final reconstruction with
377 C3 symmetry at 7.3 Å resolution based on the gold-standard Fourier shell correlation at
378 the 0.143 criterion.
379
380 **Sequence determination**
381 We re-sequenced the α-subunit gene with the same strain of *L. tarentolae* as used in
382 cryoEM sample preparation. The amino acid sequence for the LtMCC β-subunit was
383 obtained by analyzing the genome sequencing data of *L. tarentolae* Parrot Tar II (Goto
384 et al., 2020), since the putative, shotgun LtMCC β-subunit sequence on the NCBI
385 protein database was notably shorter than MCCs from other organisms, deviating from
386 the high sequence homogeneity observed across MCC sequences. A frameshift occurs
387 near the middle of the sequence, likely caused by a sequencing error. The frameshift is
388 not present in the previous genome sequencing data of *L. tarentolae* Parrot Tar II
389 (Raymond et al., 2012). Since MCC plays an essential role in the catabolism of leucine
390 across many species, it is unlikely that MCC exhibits a highly different sequence in *L.*
391 *tarentolae*.
392
393 **Atomic modeling**

394 An initial AlphaFold (Jumper et al., 2021) model prediction was generated from
395 ColabFold (Mirdita et al., 2022) using the LtMCC α-subunit and β-subunit sequences.
396 Atomic model building was conducted de novo in regions of low sequence conservation.
397 First, an individual α-subunit and β-subunit were modeled into the cryoEM map in Coot
398 (Emsley et al., 2010) and then real-space refined in Phenix (Liebschner et al., 2019).
399 The α-subunit was modeled using the α-centered map, and respectively for the β-
400 subunit. Biotin was modeled de novo into its observed density. Then, the subunits were
401 duplicated according to D3 symmetry, fitted into the cryoEM maps, and refined
402 iteratively using Phenix (Liebschner et al., 2019) and Coot (Emsley et al., 2010).
403
404 **Model analysis**
405 Buried surface area and map cross-correlation coefficient were calculated in ChimeraX
406 (Goddard et al., 2018). Binding affinity calculations were done using the PRODIGY web
407 server (Vangone and Bonvin, 2015; Xue et al., 2016). Sequence alignments and
408 similarity calculations were performed using Clustal Omega (Sievers and Higgins, 2018)
409 from the EMBL-EBI web server and visualized with ESPript 3 (Robert and Gouet, 2014).
410
411 **Data and code availability**
412 CryoEM maps of the α-subunit centered, β-subunit centered, and filament termini map
413 have been deposited in the Electron Microscopy Data Bank under accession numbers
414 EMD-XXXX, EMD-XXXX, and EMD-XXXX, respectively. The coordinates of LtMCC
415 have been deposited in the Protein Data Bank under accession number XXXX. All
416 aforementioned deposited data are publicly available as of the date of publication and

accession numbers are also listed in the key resources table. This paper does not report original code. DOIs are listed in the key resources table. This paper analyzes existing, publicly available data. These accession numbers for the datasets are listed in the key resources table. Any additional information required to reanalyze the data reported in this paper is available from the lead contact upon request.

## Acknowledgments

Our research was supported in part by grants from the U.S. National Institutes of Health (R01GM071940 to Z.H.Z., R01AI101057 to R.A., and R01GM074830 to L.H.). J.J.H. acknowledges support from STROBE NSF Science & Technology Center Grant DMR-1548924, as well as the Stone, Irving & Jean Award and the Rose Gilbert, in Memory of Maggie Gilbert Award granted by the UCLA Honors Programs. We acknowledge the use of resources at the Electron Imaging Center for Nanomachines of UCLA supported by U.S. NIH (S10RR23057 and S10OD018111) and U.S. NSF (DMR-1548924 and DBI-133813). We thank James Zhen for his advice in manuscript writing. We thank Shiqing Liao and Samuel Liu for their help with selecting curved filaments.

## Author contributions

Z.H.Z. and R.A. initiated and supervised the project. I.A. prepared the sample. C.Y. and L.H. conducted mass spectrometry. Y-T.L. carried out cryoEM imaging and data processing with assistance from J.K.J.L. and J.J.H. J.K.J.L. and J.J.H. built the atomic models. J.K.J.L., J.J.H., and Y-T.L. analyzed the data. J.J.H., J.K.J.L., and Y-T.L. made

439 illustrations and wrote the original draft. Z.H.Z., Y-T.L., J.J.H., and J.K.J.L. finalized the

440 manuscript. All authors reviewed and approved the paper.

441

442 Declaration of interests

443 The authors declare no competing interests.

444

445 **REFERENCES**


446 Amos, B., Aurrecoechea, C., Barba, M., Barreto, A., Basenko, E.Y., Bażant, W., Belnap,
447 R., Blevins, A.S., Böhme, U., Brestelli, J., et al. (2022). VEuPathDB: the eukaryotic
448 pathogen, vector and host bioinformatics resource center. Nucleic Acids Research *50*,
449 D898–D911. https://doi.org/10.1093/nar/gkab929.

450 Anderson, M.D., Che, P., Song, J., Nikolau, B.J., and Wurtele, E.S. (1998). 3-
451 Methylcrotonyl-Coenzyme A Carboxylase Is a Component of the Mitochondrial Leucine
452 Catabolic Pathway in Plants. Plant Physiology *118*, 1127–1138.
453 https://doi.org/10.1104/pp.118.4.1127.

454 Apitz-Castro, R., Rehn, K., and Lynen, F. (1970). β-Methylcrotonyl-CoA-Carboxylase.
455 European Journal of Biochemistry *16*, 71–79. https://doi.org/10.1111/j.1432-
456 1033.1970.tb01055.x.

457 Arabolaza, A., Shillito, M.E., Lin, T.-W., Diacovich, L., Melgar, M., Pham, H., Amick, D.,
458 Gramajo, H., and Tsai, S.-C. (2010). Crystal structures and mutational analyses of acyl-
459 CoA carboxylase beta subunit of Streptomyces coelicolor. Biochemistry *49*, 7367–7376.
460 https://doi.org/10.1021/bi1005305.

461 Beaty, N.B., and Lane, M.D. (1983). Kinetics of activation of acetyl-CoA carboxylase by
462 citrate. Relationship to the rate of polymerization of the enzyme. Journal of Biological
463 Chemistry *258*, 13043–13050. https://doi.org/10.1016/S0021-9258(17)44077-4.

464 Chambers, M.C., Maclean, B., Burke, R., Amodei, D., Ruderman, D.L., Neumann, S.,
465 Gatto, L., Fischer, B., Pratt, B., Egertson, J., et al. (2012). A cross-platform toolkit for
466 mass spectrometry and proteomics. Nat Biotechnol *30*, 918–920.
467 https://doi.org/10.1038/nbt.2377.

468 Chen, Y.-Y., Zhang, X.-N., Xu, C.-Z., Zhou, D.-H., Chen, J., Liu, Z.-X., sun, Y., Huang,
469 W., and Qu, L.-S. (2021). MCCC2 promotes HCC development by supporting leucine
470 oncogenic function. Cancer Cell Int *21*, 22. https://doi.org/10.1186/s12935-020-01722-
471 w.

472 Dai, W., Feng, H., and Lee, D. (2020). MCCC2 overexpression predicts poorer
473 prognosis and promotes cell proliferation in colorectal cancer. Experimental and
474 Molecular Pathology *115*, 104428. https://doi.org/10.1016/j.yexmp.2020.104428.

475 Diacovich, L., Mitchell, D.L., Pham, H., Gago, G., Melgar, M.M., Khosla, C., Gramajo,
476 H., and Tsai, S.-C. (2004). Crystal structure of the beta-subunit of acyl-CoA
477 carboxylase: structure-based engineering of substrate specificity. Biochemistry *43*,
478 14027–14036. https://doi.org/10.1021/bi049065v.

479 Diez, T.A., Wurtele, E.S., and Nikolau, B.J. (1994). Purification and Characterization of
480 3-Methylcrotonyl-Coenzyme-A Carboxylase from Leaves of Zea mays. Archives of
481 Biochemistry and Biophysics *310*, 64–75. https://doi.org/10.1006/abbi.1994.1141.

482 Emsley, P., Lohkamp, B., Scott, W.G., and Cowtan, K. (2010). Features and
483 development of *Coot*. Acta Crystallogr D Biol Crystallogr *66*, 486–501.
484 https://doi.org/10.1107/S0907444910007493.

485 Fang, L., Kaake, R.M., Patel, V.R., Yang, Y., Baldi, P., and Huang, L. (2012). Mapping
486 the Protein Interaction Network of the Human COP9 Signalosome Complex Using a
487 Label-free QTAX Strategy. Molecular & Cellular Proteomics *11*, 138–147.
488 https://doi.org/10.1074/mcp.M111.016352.

489 Fry, D.C., Fox, T., Lane, M.D., and Mildvan, A.S. (1985). NMR studies of the exchange
490 of the amide protons of d-biotin and its derivatives. Ann N Y Acad Sci *447*, 140–151.
491 https://doi.org/10.1111/j.1749-6632.1985.tb18434.x.

492 Gallardo, M.E., Desviat, L.R., Rodríguez, J.M., Esparza-Gordillo, J., Pérez-Cerdá, C.,
493 Pérez, B., Rodríguez-Pombo, P., Criado, O., Sanz, R., Morton, D.H., et al. (2001). The
494 Molecular Basis of 3-Methylcrotonylglycinuria, a Disorder of Leucine Catabolism. The
495 American Journal of Human Genetics *68*, 334–346. https://doi.org/10.1086/318202.

496 Gasteiger, E., Gattiker, A., Hoogland, C., Ivanyi, I., Appel, R.D., and Bairoch, A. (2003).
497 ExPASy: The proteomics server for in-depth protein knowledge and analysis. Nucleic
498 Acids Res *31*, 3784–3788. https://doi.org/10.1093/nar/gkg563.

499 Goddard, T.D., Huang, C.C., Meng, E.C., Pettersen, E.F., Couch, G.S., Morris, J.H.,
500 and Ferrin, T.E. (2018). UCSF ChimeraX: Meeting modern challenges in visualization
501 and analysis. Protein Sci *27*, 14–25. https://doi.org/10.1002/pro.3235.

502 Gondáš, E., Kráľová Trančíková, A., Baranovičová, E., Šofranko, J., Hatok, J.,
503 Kowtharapu, B.S., Galanda, T., Dobrota, D., Kubatka, P., Busselberg, D., et al. (2022).
504 Expression of 3-Methylcrotonyl-CoA Carboxylase in Brain Tumors and Capability to
505 Catabolize Leucine by Human Neural Cancer Cells. Cancers *14*, 585.
506 https://doi.org/10.3390/cancers14030585.

507 Goto, Y., Kuroki, A., Suzuki, K., and Yamagishi, J. (2020). Draft Genome Sequence of
508 Leishmania tarentolae Parrot Tar II, Obtained by Single-Molecule Real-Time

Sequencing. Microbiology Resource Announcements *9*, e00050-20. https://doi.org/10.1128/MRA.00050-20.

Gran, P., and Cameron-Smith, D. (2011). The actions of exogenous leucine on mTOR signalling and amino acid transporters in human myotubes. BMC Physiol *11*, 10. https://doi.org/10.1186/1472-6793-11-10.

Grünert, S.C., Stucki, M., Morscher, R.J., Suormala, T., Bürer, C., Burda, P., Christensen, E., Ficicioglu, C., Herwig, J., Kölker, S., et al. (2012). 3-methylcrotonyl-CoA carboxylase deficiency: Clinical, biochemical, enzymatic and molecular studies in 88 individuals. Orphanet J Rare Dis *7*, 31. https://doi.org/10.1186/1750-1172-7-31.

Harrison, S.C. (1996). Peptide–Surface Association: The Case of PDZ and PTB Domains. Cell *86*, 341–343. https://doi.org/10.1016/S0092-8674(00)80105-1.

He, J., Mao, Y., Huang, W., Li, M., Zhang, H., Qing, Y., Lu, S., Xiao, H., and Li, K. (2020). Methylcrotonoyl-CoA Carboxylase 2 Promotes Proliferation, Migration and Invasion and Inhibits Apoptosis of Prostate Cancer Cells Through Regulating GLUD1-P38 MAPK Signaling Pathway. OTT *Volume 13*, 7317–7327. https://doi.org/10.2147/OTT.S249906.

Ho, C.-M., Li, X., Lai, M., Terwilliger, T.C., Beck, J.R., Wohlschlegel, J., Goldberg, D.E., Fitzpatrick, A.W.P., and Zhou, Z.H. (2020). Bottom-up structural proteomics: cryoEM of protein complexes enriched from the cellular milieu. Nat Methods *17*, 79–85. https://doi.org/10.1038/s41592-019-0637-y.

Höschle, B., Gnau, V., and Jendrossek, D. 2005 (2005). Methylcrotonyl-CoA and geranyl-CoA carboxylases are involved in leucine/isovalerate utilization (Liu) and acyclic terpene utilization (Atu), and are encoded by liuB/liuD and atuC/atuF, in Pseudomonas aeruginosa. Microbiology *151*, 3649–3656. https://doi.org/10.1099/mic.0.28260-0.

Hu, Z., and Cronan, J.E. (2020). The primary step of biotin synthesis in mycobacteria. Proceedings of the National Academy of Sciences *117*, 23794–23801. https://doi.org/10.1073/pnas.2010189117.

Huang, C.S., Sadre-Bazzaz, K., Shen, Y., Deng, B., Zhou, Z.H., and Tong, L. (2010). Crystal structure of the α6β6 holoenzyme of propionyl-coenzyme A carboxylase. Nature *466*, 1001–1005. https://doi.org/10.1038/nature09302.

Huang, C.S., Ge, P., Zhou, Z.H., and Tong, L. (2012). An unanticipated architecture of the 750-kDa α6β6 holoenzyme of 3-methylcrotonyl-CoA carboxylase. Nature *481*, 219–223. https://doi.org/10.1038/nature10691.

Hunkeler, M., Hagmann, A., Stuttfeld, E., Chami, M., Guri, Y., Stahlberg, H., and Maier, T. (2018). Structural basis for regulation of human acetyl-CoA carboxylase. Nature *558*, 470–474. https://doi.org/10.1038/s41586-018-0201-4.

Ingerson-Mahar, M., Briegel, A., Werner, J.N., Jensen, G.J., and Gitai, Z. (2010). The metabolic enzyme CTP synthase forms cytoskeletal filaments. Nat Cell Biol *12*, 739–746. https://doi.org/10.1038/ncb2087.

Jumper, J., Evans, R., Pritzel, A., Green, T., Figurnov, M., Ronneberger, O., Tunyasuvunakool, K., Bates, R., Žídek, A., Potapenko, A., et al. (2021). Highly accurate protein structure prediction with AlphaFold. Nature *596*, 583–589. https://doi.org/10.1038/s41586-021-03819-2.

Kim, C.-W., Moon, Y.-A., Park, S.W., Cheng, D., Kwon, H.J., and Horton, J.D. (2010). Induced polymerization of mammalian acetyl-CoA carboxylase by MIG12 provides a tertiary level of regulation of fatty acid synthesis. Proceedings of the National Academy of Sciences *107*, 9626–9631. https://doi.org/10.1073/pnas.1001292107.

Kim, S.-Y., Kim, Y.-W., Hegerl, R., Cyrklaff, M., and Kim, I.-S. (2005). Novel type of enzyme multimerization enhances substrate affinity of oat β-glucosidase. Journal of Structural Biology *150*, 1–10. https://doi.org/10.1016/j.jsb.2004.07.007.

Kim, Y.-M., Seo, G.H., Kim, G.-H., Yoo, H.-W., and Lee, B.H. (2017). Novel heterozygous *MCCC1* mutations identified in a patient with 3-methylcrotonyl-coenzyme A carboxylase deficiency. J Genet Med *14*, 23–26. https://doi.org/10.5734/JGM.2017.14.1.23.

Kleinschmidt, A.K., Moss, J., and Lane, D.M. (1969). Acetyl coenzyme A carboxylase: filamentous nature of the animal enzymes. Science *166*, 1276–1278. https://doi.org/10.1126/science.166.3910.1276.

Knappe, J., Schlegel, H.G., and Lynen, F. (1961). [On the biochemical function of biotin. I. The participation of beta-methyl-crotonyl-carboxylase in the formation of beta-hydroxy-beta-methyl-glutaryl-CoA from beta-hydroxy-isovaleryl-CoA]. Biochem Z *335*, 101–122. .

Knowles, J.R. (1989). The Mechanism of Biotin-Dependent Enzymes. Annual Review of Biochemistry *58*, 195–221. https://doi.org/10.1146/annurev.bi.58.070189.001211.

Kremer, J.R., Mastronarde, D.N., and McIntosh, J.R. (1996). Computer Visualization of Three-Dimensional Image Data Using IMOD. Journal of Structural Biology *116*, 71–76. https://doi.org/10.1006/jsbi.1996.0013.

Kucukelbir, A., Sigworth, F.J., and Tagare, H.D. (2014). Quantifying the local resolution of cryo-EM density maps. Nat Methods *11*, 63–65. https://doi.org/10.1038/nmeth.2727.

Lee, S.H., and Hong, Y.H. (2014). Asymptomatic maternal 3-methylcrotonylglycinuria detected by her unaffected baby's neonatal screening test. Korean J Pediatr *57*, 329. https://doi.org/10.3345/kjp.2014.57.7.329.

Liebschner, D., Afonine, P.V., Baker, M.L., Bunkóczi, G., Chen, V.B., Croll, T.I., Hintze, B., Hung, L.-W., Jain, S., McCoy, A.J., et al. (2019). Macromolecular structure

determination using X-rays, neutrons and electrons: recent developments in Phenix. Acta Cryst D *75*, 861–877. https://doi.org/10.1107/S2059798319011471.

Liu, Y., Yuan, Z., and Song, C. (2019). Methylcrotonoyl-CoA carboxylase 2 overexpression predicts an unfavorable prognosis and promotes cell proliferation in breast cancer. Biomark Med *13*, 427–436. https://doi.org/10.2217/bmm-2018-0475.

Lynch, E.M., Hicks, D.R., Shepherd, M., Endrizzi, J.A., Maker, A., Hansen, J.M., Barry, R.M., Gitai, Z., Baldwin, E.P., and Kollman, J.M. (2017). Human CTP synthase filament structure reveals the active enzyme conformation. Nat Struct Mol Biol *24*, 507–514. https://doi.org/10.1038/nsmb.3407.

Lynen, F., Knappe, J., Lorch, E., Juetting, G., Ringelmann, E., and Lachance, J.P. (1961). [On the biochemical function of biotin. II. Purification and mode of action of beta-methyl-crotonyl-carboxylase]. Biochem Z *335*, 123–167. .

Mastronarde, D.N. (2005). Automated electron microscope tomography using robust prediction of specimen movements. Journal of Structural Biology *152*, 36–51. https://doi.org/10.1016/j.jsb.2005.07.007.

Mattei, S., Ban, A., Picenoni, A., Leibundgut, M., Glockshuber, R., and Boehringer, D. (2020). Structure of native glycolipoprotein filaments in honeybee royal jelly. Nat Commun *11*, 6267. https://doi.org/10.1038/s41467-020-20135-x.

Maud, H., Noé, P.T., Pauline, D., Sandra, S., Violette, M., Anne-Lise, S., Bell Jason, C., Emmanuel, M., Stephen, K., Le Cam, E., et al. (2022). Assembly mechanism and cryoEM structure of RecA recombination nucleofilaments from *Streptococcus pneumoniae* (Microbiology).

Maurice, M.St., Reinhardt, L., Surinya, K.H., Attwood, P.V., Wallace, J.C., Cleland, W.W., and Rayment, I. (2007). Domain Architecture of Pyruvate Carboxylase, a Biotin-Dependent Multifunctional Enzyme. Science *317*, 1076–1079. https://doi.org/10.1126/science.1144504.

Meredith, M.J., and Lane, M.D. (1978). Acetyl-CoA carboxylase. Evidence for polymeric filament to protomer transition in the intact avian liver cell. Journal of Biological Chemistry *253*, 3381–3383. https://doi.org/10.1016/S0021-9258(17)34809-3.

Mirdita, M., Schütze, K., Moriwaki, Y., Heo, L., Ovchinnikov, S., and Steinegger, M. (2022). ColabFold: making protein folding accessible to all. Nat Methods *19*, 679–682. https://doi.org/10.1038/s41592-022-01488-1.

Moss, J., and Lane, M.D. (1971). The Biotin-Dependent Enzymes. In Advances in Enzymology and Related Areas of Molecular Biology, (John Wiley & Sons, Ltd), pp. 321–442.

Nikolau, B.J., Ohlrogge, J.B., and Wurtele, E.S. (2003). Plant biotin-containing carboxylases. Archives of Biochemistry and Biophysics *414*, 211–222. https://doi.org/10.1016/S0003-9861(03)00156-5.

Park, C.K., and Horton, N.C. (2019). Structures, functions, and mechanisms of filament forming enzymes: a renaissance of enzyme filamentation. Biophys Rev *11*, 927–994. https://doi.org/10.1007/s12551-019-00602-6.

Park, S., Hwang, I.-W., Makishima, Y., Perales-Clemente, E., Kato, T., Niederländer, N.J., Park, E.Y., and Terzic, A. (2013). Spot14/Mig12 heterocomplex sequesters polymerization and restrains catalytic function of human acetyl-CoA carboxylase 2. Journal of Molecular Recognition *26*, 679–688. https://doi.org/10.1002/jmr.2313.

Parrot, L. (1949). Sur quelques souches de Leishmania. Archives de l'Institut Pasteur d'Algerie *1949*, 106–109. .

Paulussen, K.J.M., McKenna, C.F., Beals, J.W., Wilund, K.R., Salvador, A.F., and Burd, N.A. (2021). Anabolic Resistance of Muscle Protein Turnover Comes in Various Shapes and Sizes. Front. Nutr. *8*, 615849. https://doi.org/10.3389/fnut.2021.615849.

Pelletier, M., Read, L.K., and Aphasizhev, R. (2007). Isolation of RNA Binding Proteins Involved in Insertion/Deletion Editing. In Methods in Enzymology, (Elsevier), pp. 75–105.

Pfab, J., Phan, N.M., and Si, D. (2021). DeepTracer for fast de novo cryo-EM protein structure modeling and special studies on CoV-related complexes. Proceedings of the National Academy of Sciences *118*, e2017525118. https://doi.org/10.1073/pnas.2017525118.

Polley, S., Lyumkis, D., and Horton, N.C. (2019). Mechanism of Filamentation-Induced Allosteric Activation of the SgrAI Endonuclease. Structure *27*, 1497-1507.e3. https://doi.org/10.1016/j.str.2019.08.001.

Raymond, F., Boisvert, S., Roy, G., Ritt, J.-F., Légaré, D., Isnard, A., Stanke, M., Olivier, M., Tremblay, M.J., Papadopoulou, B., et al. (2012). Genome sequencing of the lizard parasite Leishmania tarentolae reveals loss of genes associated to the intracellular stage of human pathogenic species. Nucleic Acids Research *40*, 1131–1147. https://doi.org/10.1093/nar/gkr834.

Robert, X., and Gouet, P. (2014). Deciphering key features in protein structures with the new ENDscript server. Nucleic Acids Research *42*, W320–W324. https://doi.org/10.1093/nar/gku316.

Scheffen, M., Marchal, D.G., Beneyton, T., Schuller, S.K., Klose, M., Diehl, C., Lehmann, J., Pfister, P., Carrillo, M., He, H., et al. (2021). A new-to-nature carboxylation module to improve natural and synthetic CO2 fixation. Nat Catal *4*, 105–115. https://doi.org/10.1038/s41929-020-00557-y.

654 Sievers, F., and Higgins, D.G. (2018). Clustal Omega for making accurate alignments of
655 many protein sequences. Protein Sci *27*, 135–145. https://doi.org/10.1002/pro.3290.

656 Tong, L. (2013). Structure and function of biotin-dependent carboxylases. Cell Mol Life
657 Sci *70*, 863–891. https://doi.org/10.1007/s00018-012-1096-0.

658 Vangone, A., and Bonvin, A.M. (2015). Contacts-based prediction of binding affinity in
659 protein–protein complexes. ELife *4*, e07454. https://doi.org/10.7554/eLife.07454.

660 Waldrop, G.L., Holden, H.M., and Maurice, M.St. (2012). The enzymes of biotin
661 dependent $CO_2$ metabolism: What structures reveal about their reaction mechanisms:
662 Biotin Dependent Enzymes. Protein Science *21*, 1597–1619.
663 https://doi.org/10.1002/pro.2156.

664 Wang, F., Gu, Y., O'Brien, J.P., Yi, S.M., Yalcin, S.E., Srikanth, V., Shen, C., Vu, D.,
665 Ing, N.L., Hochbaum, A.I., et al. (2019). Structure of Microbial Nanowires Reveals
666 Stacked Hemes that Transport Electrons over Micrometers. Cell *177*, 361-369.e10.
667 https://doi.org/10.1016/j.cell.2019.03.029.

668 Webb, B.A., Dosey, A.M., Wittmann, T., Kollman, J.M., and Barber, D.L. (2017). The
669 glycolytic enzyme phosphofructokinase-1 assembles into filaments. J Cell Biol *216*,
670 2305–2313. https://doi.org/10.1083/jcb.201701084.

671 Wei, J., and Tong, L. (2015). Crystal structure of the 500-kDa yeast acetyl-CoA
672 carboxylase holoenzyme dimer. Nature *526*, 723–727.
673 https://doi.org/10.1038/nature15375.

674 Wei, J., and Tong, L. (2018). How Does Polymerization Regulate Human Acetyl-CoA
675 Carboxylase 1? Biochemistry *57*, 5495–5496.
676 https://doi.org/10.1021/acs.biochem.8b00881.

677 Xiang, S., and Tong, L. (2008). Crystal structures of human and Staphylococcus aureus
678 pyruvate carboxylase and molecular insights into the carboxyltransfer reaction. Nat
679 Struct Mol Biol *15*, 295–302. https://doi.org/10.1038/nsmb.1393.

680 Xue, L.C., Rodrigues, J.P., Kastritis, P.L., Bonvin, A.M., and Vangone, A. (2016).
681 PRODIGY: a web server for predicting the binding affinity of protein–protein complexes.
682 Bioinformatics *32*, 3676–3678. https://doi.org/10.1093/bioinformatics/btw514.

683 Yang, J., Chi, Y., Burkhardt, B.R., Guan, Y., and Wolf, B.A. (2010). Leucine metabolism
684 in regulation of insulin secretion from pancreatic beta cells: Nutrition Reviews©, Vol. 68,
685 No. 5. Nutrition Reviews *68*, 270–279. https://doi.org/10.1111/j.1753-
686 4887.2010.00282.x.

687 Zhang, K. (2016). Gctf: Real-time CTF determination and correction. J Struct Biol *193*,
688 1–12. https://doi.org/10.1016/j.jsb.2015.11.003.

Zheng, S.Q., Palovcak, E., Armache, J.-P., Verba, K.A., Cheng, Y., and Agard, D.A. (2017). MotionCor2: anisotropic correction of beam-induced motion for improved cryo-electron microscopy. Nat Methods *14*, 331–332. https://doi.org/10.1038/nmeth.4193.

Zivanov, J., Nakane, T., Forsberg, B.O., Kimanius, D., Hagen, W.J., Lindahl, E., and Scheres, S.H. (2018). New tools for automated high-resolution cryo-EM structure determination in RELION-3. ELife *7*, e42166. https://doi.org/10.7554/eLife.42166.

# FIGURES

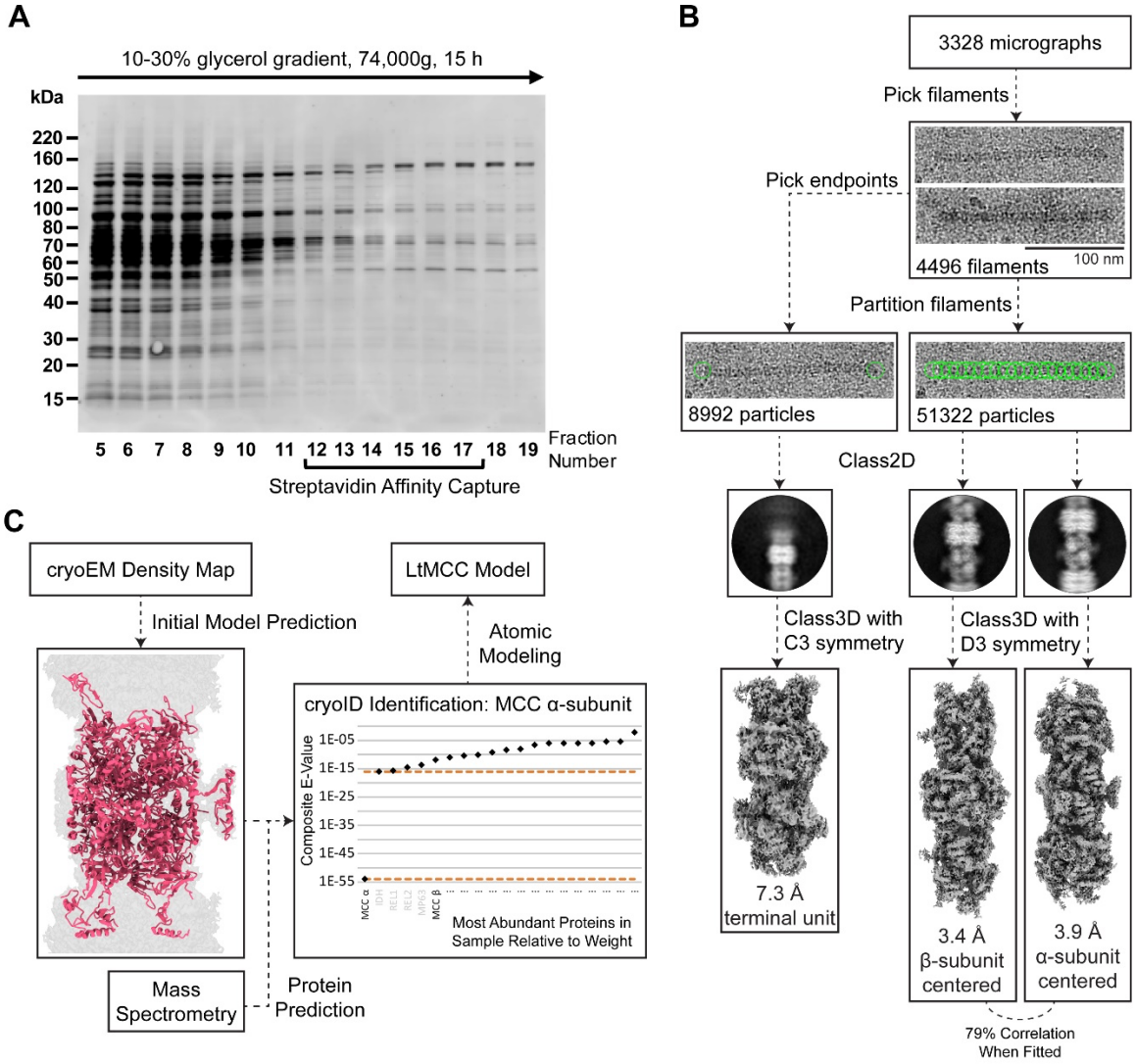


**Figure 1. Discovery of filamentous 3-methylcrotonyl-CoA carboxylase from mitochondria of *L. tarentolae***

(A) Sodium dodecyl sulfate–polyacrylamide gel electrophoresis (SDS-PAGE) of the glycerol gradient fractions obtained from mitochondrial lysate. The gel was stained by Sypro Ruby.

(B) Workflow for cryoEM imaging and reconstruction. Filaments observed in cryoEM micrographs were visually identified, partitioned into segments of equal length, classified in 2D and 3D. Refinement of 3D reconstructions yielded an α-centered and β-centered cryoEM map. The filament ends were picked and reconstructed similarly, converging into a single map for both ends of the filament (i.e., the termini map).

(C) Workflow for protein identification and atomic modeling. From an input cryoEM map, DeepTracer (Pfab et al., 2021) generated an initial model with predicted amino acid sequence, which was input into cryoID (Ho et al., 2020) together with mass spectrometry data. CryoID predicted that the filaments contained LtMCC. Finally, de novo atomic modeling of LtMCC was performed in Coot (Emsley et al., 2010) using an AlphaFold predicted model as a reference (Jumper et al., 2021; Mirdita et al., 2022).

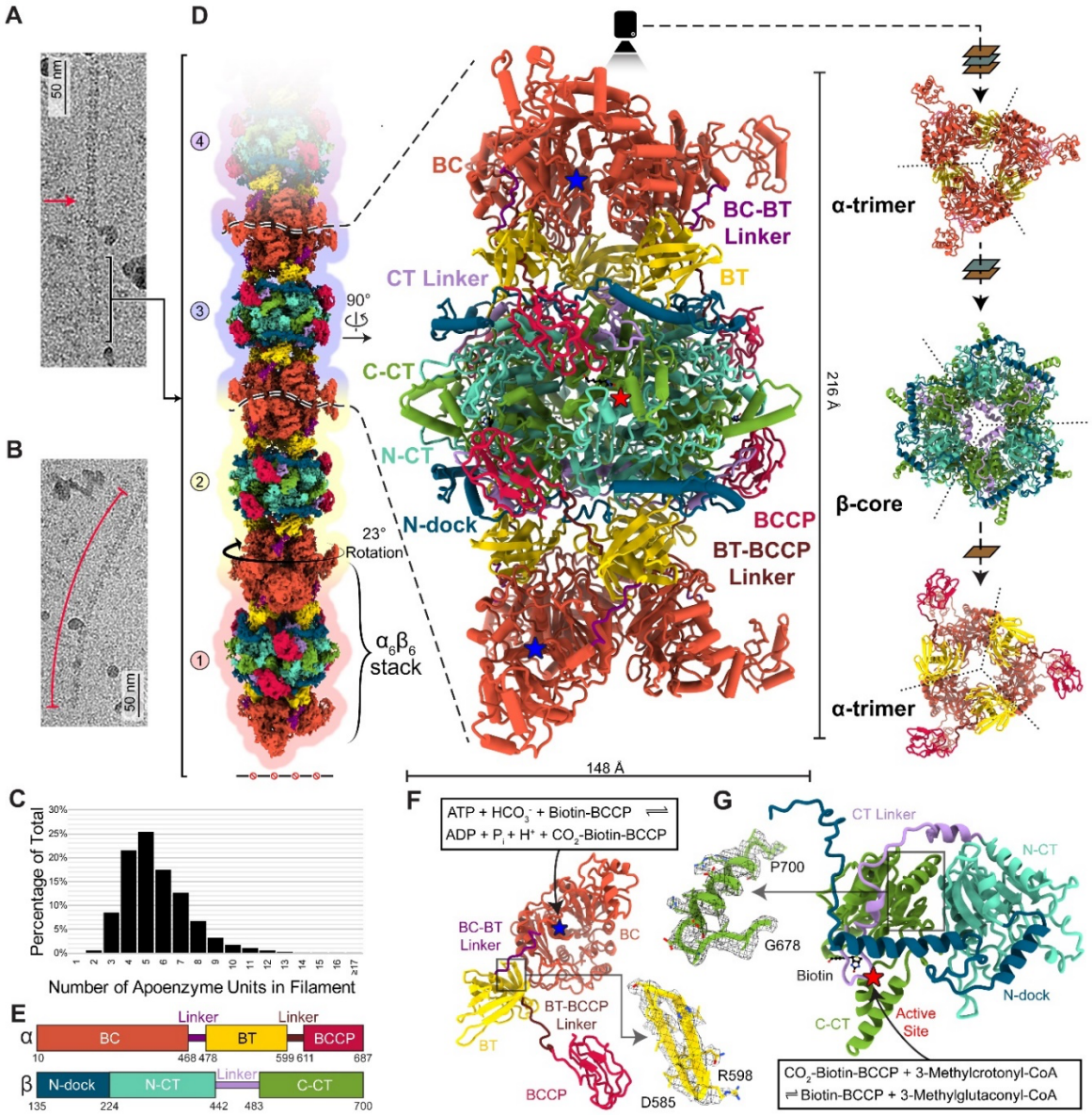


**Figure 2. Structure of the filamentous LtMCC**

(A-C) CryoEM images of a straight (A) and curved (B) LtMCC filament, and distribution of filament lengths (C).

(D-E) CryoEM map and atomic models of the LtMCC filament. The composite cryoEM map of the filament (left column in D) is composed of three copies of the α-centered map, three copies of the β-centered map, and one copy of the termini map, with overlapping subunits. The atomic models (middle and right columns in D) of an $\alpha_6\beta_6$ dodecamer and its trimeric stacks are shown in various views as ribbons, colored by domains according to the scheme in (E). The view directions are indicated by arrows, planes, and the camera. The dashed lines in the right column demarcate the boundaries between neighboring subunits (β-core is two-layered).

(F-G) Atomic model of an α-subunit (F) and a β-subunit (G) of LtMCC shown as ribbons colored by domains with active sites labeled. Insets: example cryoEM densities superimposed with the atomic model.

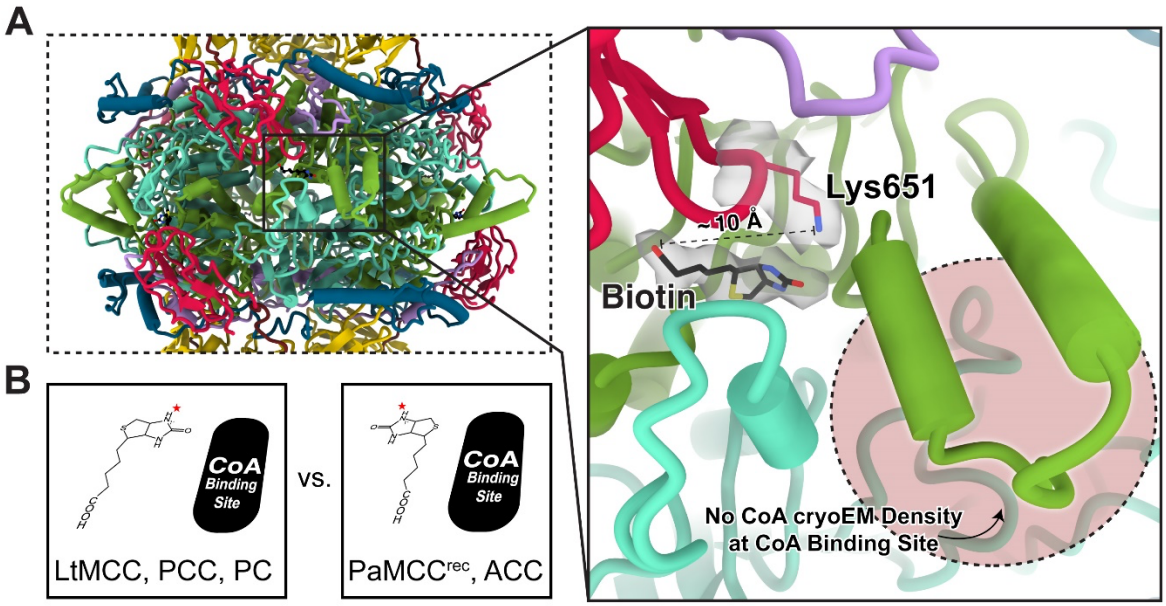


**Figure 3. Presence of non-covalently bound biotin and lack of CoA in the LtMCC filament**

(A) Close-up view of the middle column of Figure 2D, showing the biotin-containing site surrounded by the CT linker (purple), the BCCP (red), N-CT (turquoise), and C-CT (green) domains. The conserved Lys651 (red) and the non-covalently bound biotin (black) are shown as sticks, superimposed with their cryoEM densities (semi-transparent gray). The distance between the carboxyl group of biotin and the ε-amino group of Lys651 is about 10 Å. Notably, the CoA binding site (pink circle region) lacks cryoEM density, indicating absence of CoA.

(B) Comparison of biotin and CoA orientations documented in various carboxylases (Fry et al., 1985; Huang et al., 2010, 2012; Scheffen et al., 2021; Wei and Tong, 2015). The red star indicates the location of the N1′ atom of biotin.

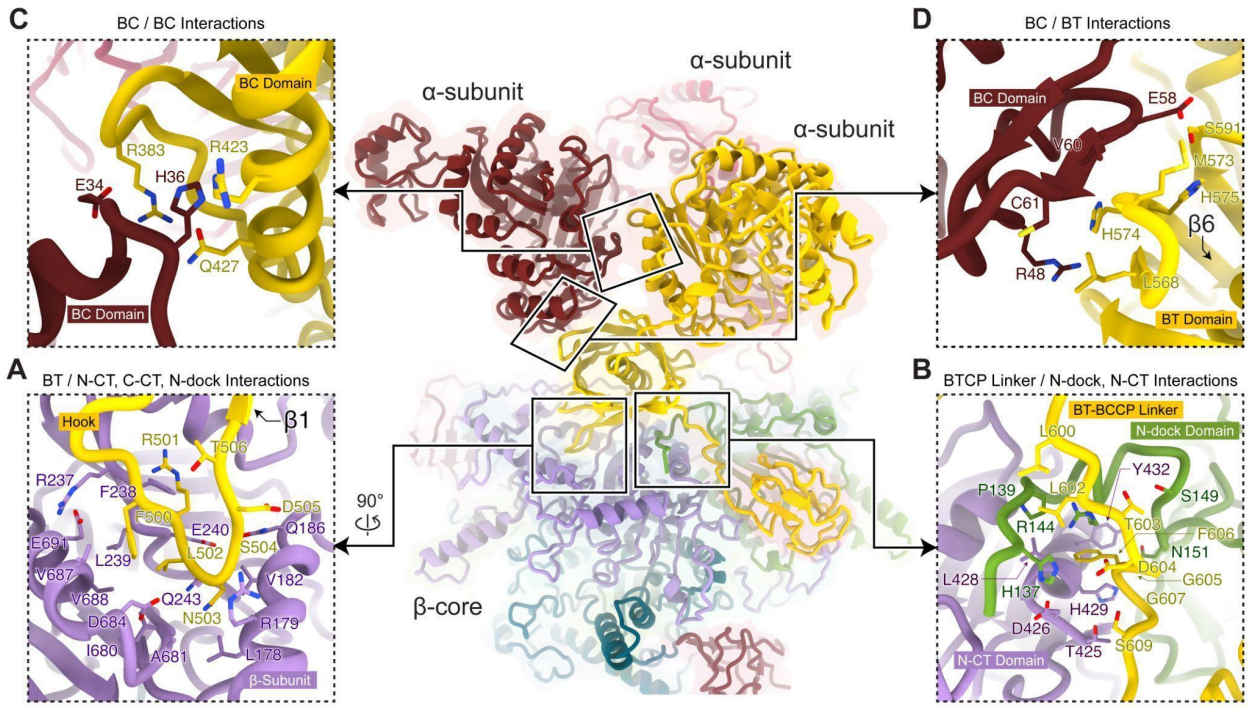


**Figure 4. Subunit interactions in the filamentous LtMCC**

Interacting regions are boxed and examined in close-up views (A-D) with their interfacial residues labeled. Interactions between α- and β-subunits (A-B) are more extensive than interactions among α-subunits (C-D).

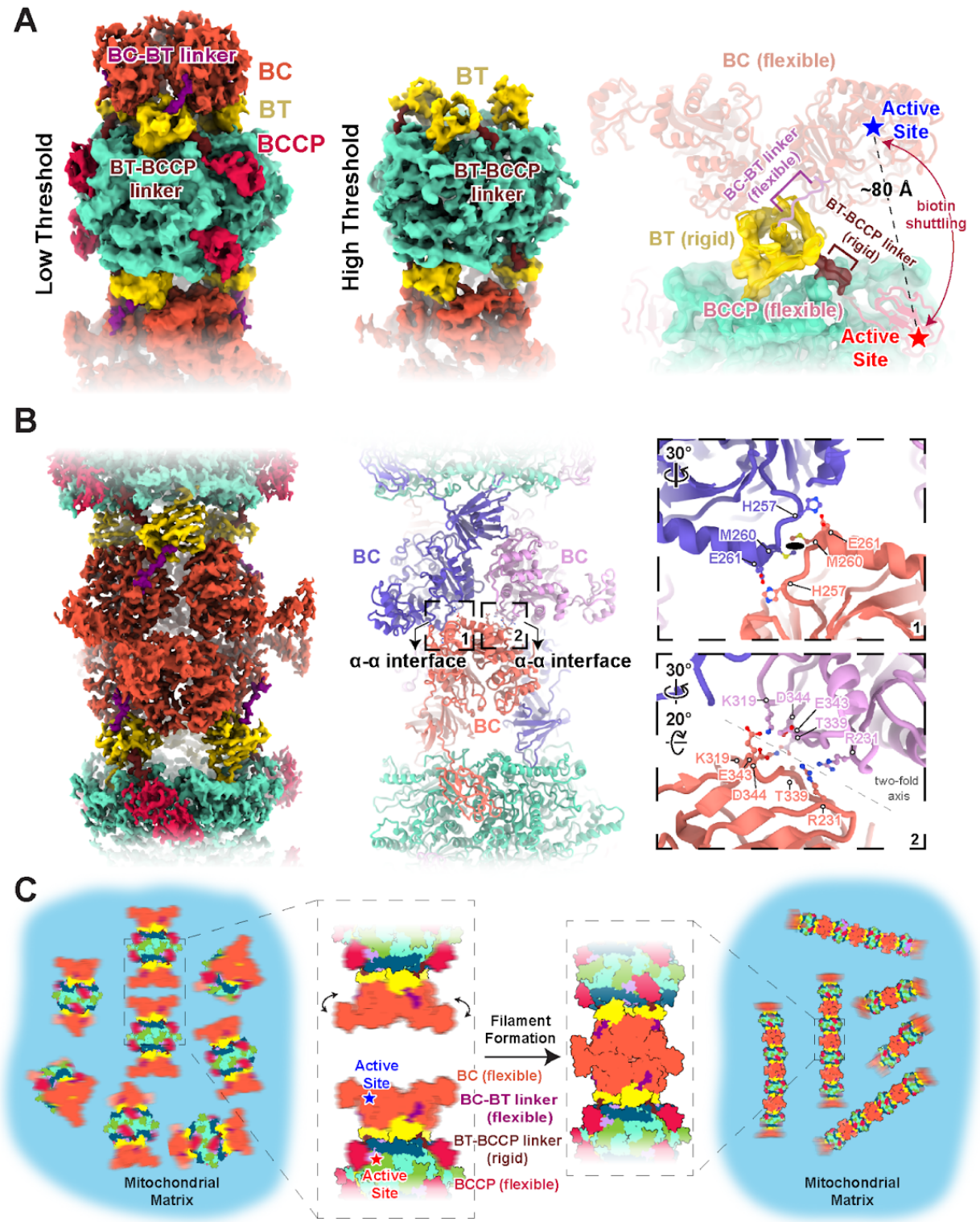


**Figure 5. Filament formation stabilizes flexible BCCP and BT domains in LtMCC**
(A) Structure of the filament termini. The left and middle panels show the 7.3 Å cryoEM map of the filament termini at a low and high density threshold, respectively. The α-subunit is colored by domain according to the scheme in Figure 2E and the entire β-core is turquoise. Note, while visible at low threshold, the BCCP and BC domain

753 densities disappear at high threshold. The right panel shows the atomic model of the
754 filament terminus with the rigid and flexible domains in harder and softer shades,
755 respectively.
756 (B) Structure of the α-α interface in the LtMCC filament. The cryoEM map (left panel) is
757 colored as in (A) but the atomic models (middle panel) of the interfacing α-subunits are
758 colored differently from each other to delineate individual α-subunits. Close-up views
759 (right panel) of the two boxed areas in the middle panel show interfacing residues at the
760 α-α interface. The ellipse in the top right panel denotes the local two-fold symmetry axis.
761 (C) Proposed model of filament formation and stabilization. Blurry domains indicate their
762 flexibility.

763 # TABLES

764 **Table 1. CryoEM map and model statistics.**

| | α-subunit centered map | β-subunit centered map | Termini map |
|---|---|---|---|
| **Data collection and processing** | | | |
| Magnification | 81,000 | 81,000 | 81,000 |
| Voltage (kV) | 300 | 300 | 300 |
| Electron exposure ($e^-$/Å$^2$) | 40 | 40 | 40 |
| Defocus range (μm) | -1.5 to -2.5 | -1.5 to -2.5 | -1.5 to -2.5 |
| Pixel size (Å) | 1.1 | 1.1 | 1.1 |
| Symmetry imposed | D3 | D3 | C3 |
| Initial particle images (no.) | 51,322 | 51,322 | 8,992 |
| Final particle images (no.) | 7,582 | 13,250 | 3,380 |
| Map resolution (Å) | 3.9 | 3.4 | 7.3 |
| FSC threshold | 0.143 | 0.143 | 0.143 |
| Estimated resolution range (Å) | 3-5 | 3-5 | 6-8 |
| Map sharpening B factor (Å$^2$) | -112 | -85 | -153 |
| **Model refinement** | | | |
| Model-to-map fit, mask CC | 0.47 | 0.62 | 0.02 |
| Model composition | | | |
| Non-hydrogen atoms | 57846 | 57846 | 57846 |
| Protein residues | 7464 | 7464 | 7464 |
| Ligands | BTI: 6 | BTI: 6 | BTI: 6 |
| Mean isotropic B factor (Å$^2$) | | | |
| Protein | 70.80 | 70.80 | 70.80 |
| Ligand | 150.43 | 150.43 | 150.43 |
| R.M.S. deviations | | | |
| Bond lengths (Å) | 0.006 | 0.006 | 0.006 |
| Bond angles (°) | 1.089 | 1.088 | 1.089 |
| Validation | | | |

| | | | |
|---|---|---|---|
| MolProbity score | 2.35 | 2.35 | 2.35 |
| Clashscore | 21.26 | 21.31 | 21.29 |
| Rotamer outliers (%) | 0.39 | 0.39 | 0.39 |
| Ramachandran statistics | | | |
| Outliers (%) | 0.00 | 0.00 | 0.00 |
| Allowed (%) | 9.40 | 9.38 | 9.38 |
| Favored (%) | 90.60 | 90.62 | 90.62 |

765

# SUPPLEMENTAL FIGURES

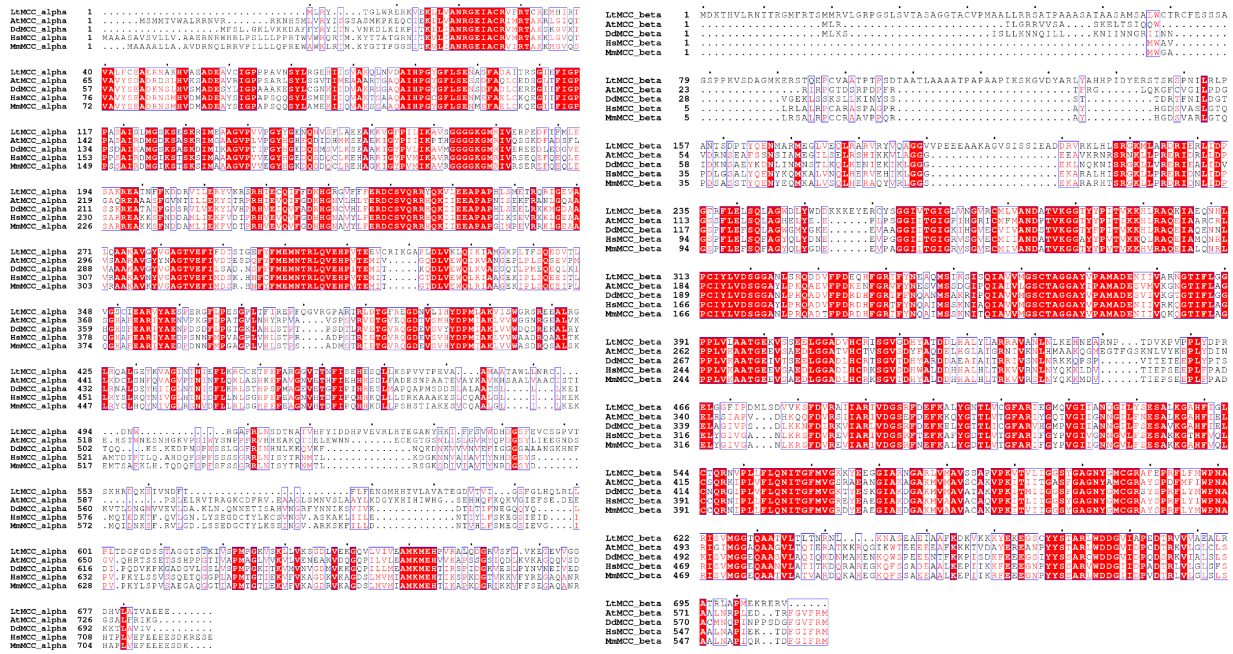


**Figure S1. Multiple sequence alignment from *ESPript 3.0* (Robert and Gouet, 2014).**

Left panel compares LtMCC α-subunit with α-subunits from *Arabidopsis thaliana* MCC (AtMCC), *Dictyostelium discoideum* MCC (DdMCC), *Homo sapien* MCC (HsMCC), and *Mus Musculus* MCC (MmMCC). Right panel compares LtMCC β-subunit with β-subunits from AtMCC, DdMCC, HsMCC, and MmMCC. Boxes with and without solid red background indicate identical residues and similar residues, respectively. Dots on top of the residues demarcate intervals of ten residues.

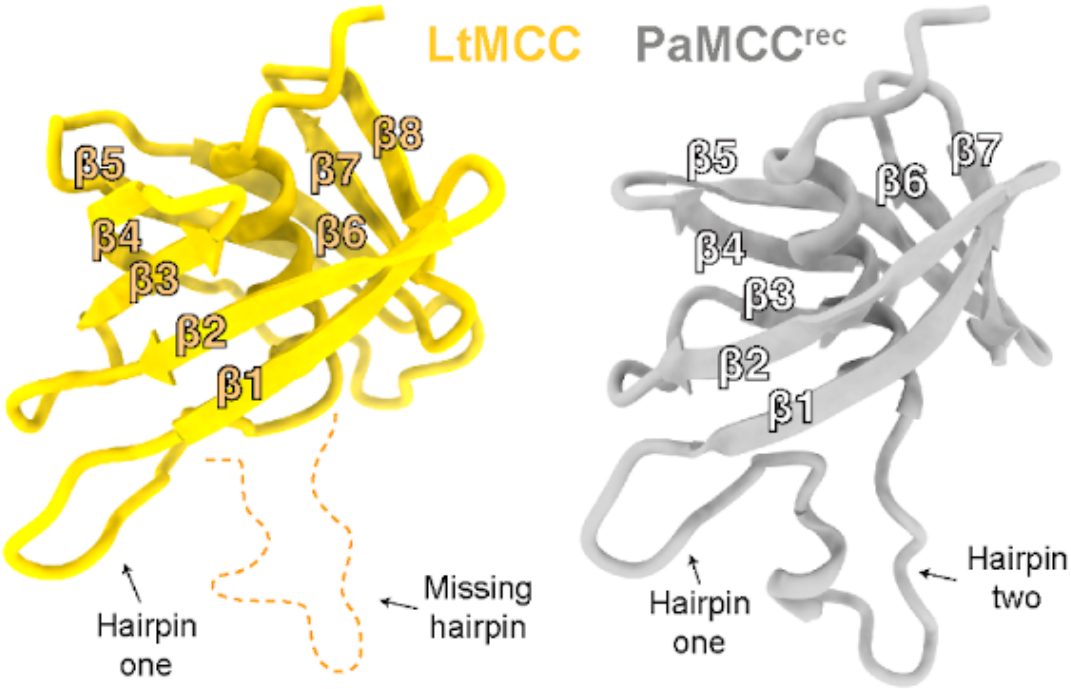


**Figure S2. Structural comparison of the BT domain from LtMCC and PaMCC$^{rec}$**
The LtMCC BT domain exhibits an 8-stranded β-sheet fold while the PaMCC$^{rec}$ BT domain contains a 7-stranded β-sheet fold. The PaMCC$^{rec}$ BT domain possesses a hook with two hairpins. The LtMCC BT domain possesses a hook with only one hairpin.

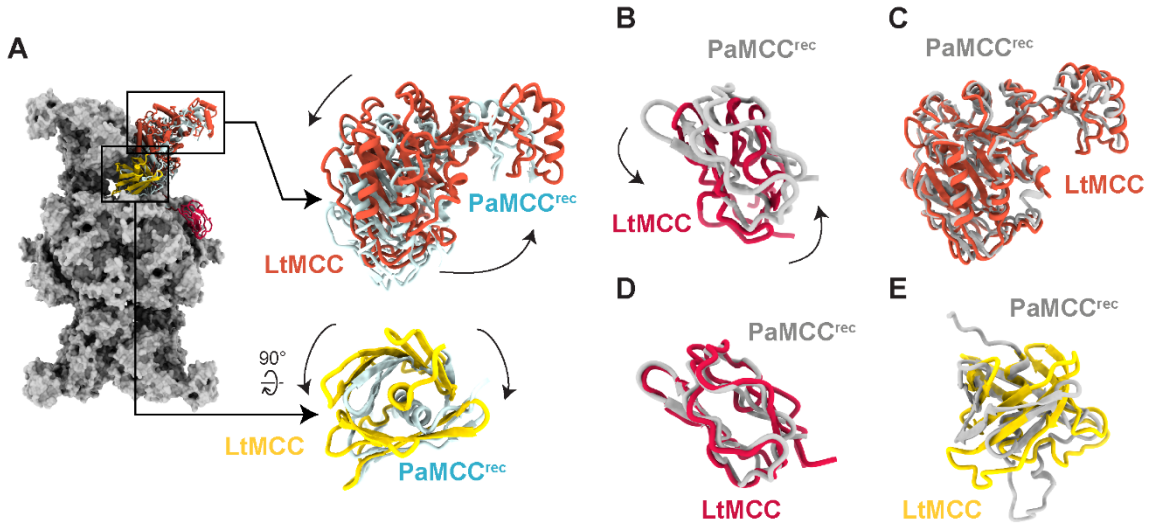


**Figure S3. Structural comparison of PaMCC$^{rec}$ and LtMCC**

(A-B) Mismatched domain structures when the PaMCC$^{rec}$ and LtMCC $\alpha_6\beta_6$ dodecamers are superimposed globally. PaMCC$^{rec}$ apoenzyme (A) and holoenzyme (B) are globally superimposed with the LtMCC dodecamer. In (A), the BC and BT domains are rotated in LtMCC compared to the PaMCC$^{rec}$ apoenzyme, as indicated by arrows. The BCCP domain is unmodeled in the PaMCC$^{rec}$ apoenzyme. The entire PaMCC$^{rec}$ apoenzyme is shown as a gray surface. In (B), the BCCP domain in LtMCC is rotated relative to the BCCP domain in the PaMCC$^{rec}$ holoenzyme, as indicated by arrows.

(C-E) Matched domain structures when individual domains from PaMCC$^{rec}$ and LtMCC are superimposed locally. BC (C), BCCP (D), and BT (E) domains from the two dodecamers are treated as individual models and superimposed independent from the global dodecameric structure.

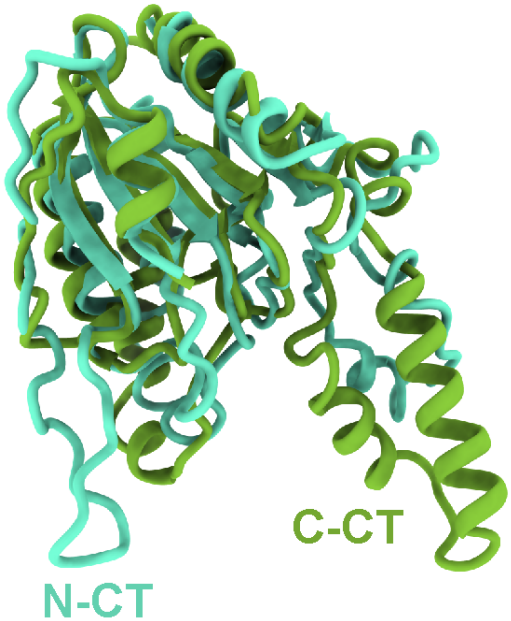


**Figure S4. The N-CT and C-CT domain local alignment for LtMCC**
The N-CT and C-CT domains are homologous, despite low sequence similarity.

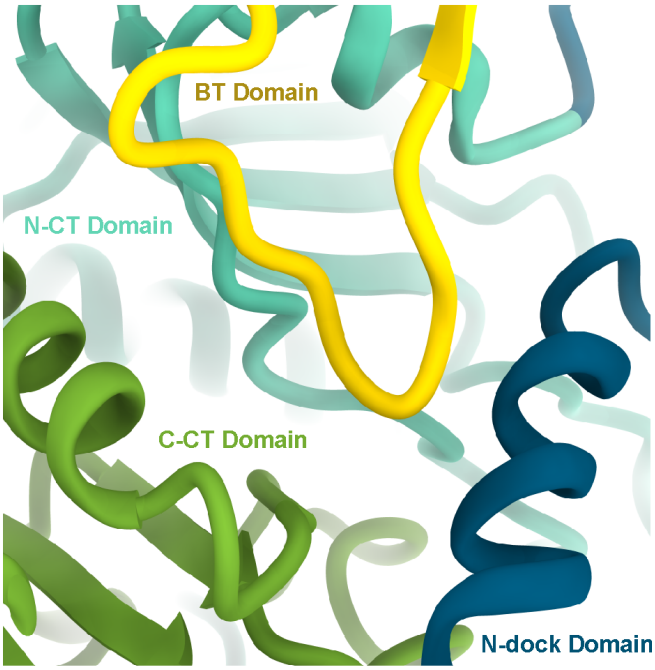


**Figure S5. Close-up view of the α-subunit BT hook interacting with the domains that make up the β-subunit groove**

The BT hook is colored yellow. The N-CT, C-CT, and N-dock domains from the same β-subunit make up the β-subunit groove. The N-CT domain is colored in light blue, the C-CT domain is colored in green, and the N-dock domain is colored in dark blue.

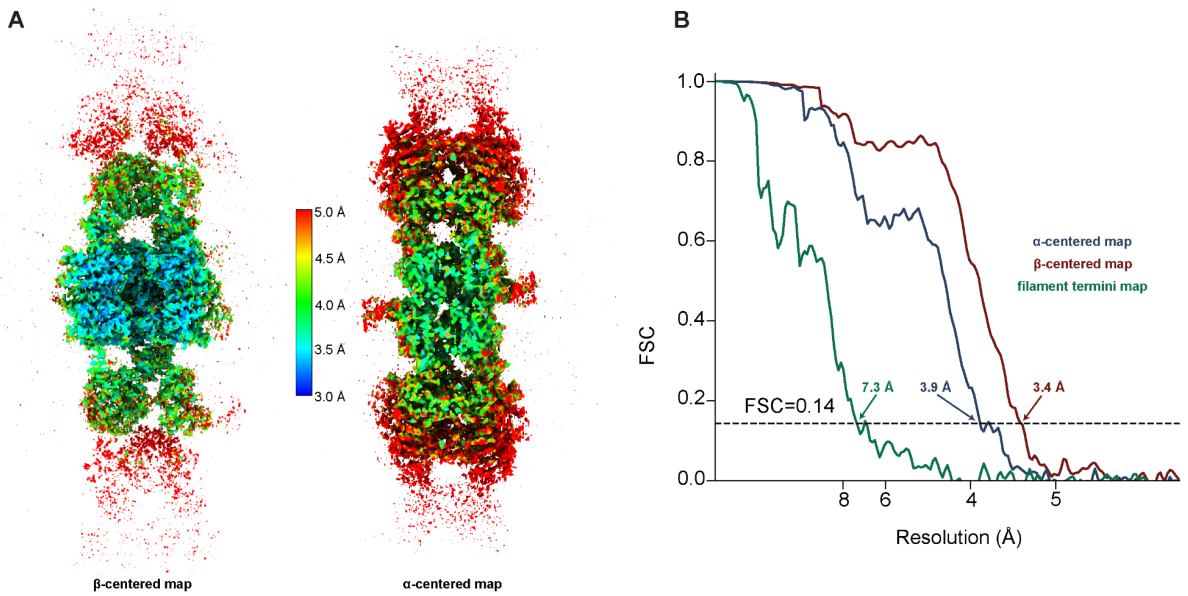


**Figure S6. Resolution evaluation of cryoEM reconstruction for LtMCC filaments**
(A) Local resolution evaluation by ResMap (Kucukelbir et al., 2014) for the α-centered and β-centered cryoEM maps of LtMCC filaments. The color key between the two maps shows their coloring by resolution.
(B) FSC curves of the final α-centered, β-centered, and filament termini cryoEM maps.

809 **Supplemental Video Legends**
810
811 Video S1. Ribbon diagram of an $\alpha_6\beta_6$ dodecamer of the filamentous LtMCC, showing
812 the α-trimer and β-core layers, related to Figure 2D.
813
814 Video S2. LtMCC filamentation stabilizes the BC domain, related to Figure 5.
815
816 **Supplemental Table Legends**
817
818 Table S1. Mass spectrometry data with LtMCC subunits colored in red